MRS Communications (2018), *8*, 809–822
© Materials Research Society, 2018
doi:10.1557/mrc.2018.106

MRS Communications

Prospective Article

Boosting interfacial charge transfer for efficient water-splitting photoelectrodes: progress in bismuth vanadate photoanodes using various strategies

Taemin Ludvic Kim*, Min-Ju Choi*, and **Ho Won Jang,** Department of Materials Science and Engineering, Research Institute of Advanced Materials, Seoul National University, Seoul 08826, Republic of Korea

Address all correspondence to Ho Won Jang at **hwjang@snu.ac.kr**

(Received 30 April 2018; accepted 30 May 2018)

Abstract

Bismuth vanadate ($BiVO_4$) is regarded as a viable material for water oxidation due to various benefits such as visible light absorption, low production cost, and resistance to photocorrosion. Recently, numerous attempts have been adopted to improve the performance of $BiVO_4$. In this work, we highlight the important strategies that have been made for improving the performance of the photoanode material, such as fabricating nanostructured electrode, controlling reacting facet, stacking with other materials, utilizing plasmonics, loading co-catalyst, and controlling the interfacial band bending with ferroelectrics. Taking advantage of the strategies, highly efficient $BiVO_4$ photoelectrodes could be demonstrated. Finally, we discuss the perspective of $BiVO_4$-based photoanodes.

Introduction

Since Fujishima and Honda discovered photoelectrochemical water splitting with *n*-type TiO_2 electrodes in 1972,[1] overwhelming attention has been focused on photoelectrolysis of water to oxygen and hydrogen in the past decades[2–10] due to the increasing demand on sustainable energy supply and environmental protection.[11, 12] The solar energy-based water splitting is one of the attractive technologies to prevent environmental pollution and overcome the global energy crisis[13–16] owing to its non-toxicity and sustainability. Photoelectrochemical water splitting is a carbon-free reaction that reduces water to hydrogen in photocathode and oxidizes water to oxygen in photoanode. Among the two cathodic and anodic reactions that take place in each electrode, photoanodic water oxidation is particularly challenging and requires high overpotentials due to the slow kinetics with multi-electron transfer.[17, 18] Thus, research on photoanode that can oxidize water to oxygen in a stable way is crucial for commercially available photoelectrochemical cells (PECs).

Water oxidation in photoanode involves multiple steps including light absorption, charge separation, transportation, and charge injection to water.[19–22] Therefore, desirable photoanodes should have a properly small band gap to absorb sunlight and generate electron–hole pair, sufficient carrier lifetime and efficient charge separation to suppress recombination, and thermodynamically favorable valence band edge position that provides sufficient overpotential for charge injection to water.[23] In principle, TiO_2 can only utilize <5% of the solar energy due to the wide bandgap (3–3.2 eV), which restricts its potential application. Thus, as an alternative, various *n*-type semiconductors have been investigated with these requirements.[3, 5, 9, 10, 18, 24] Among them, bismuth vanadate ($BiVO_4$) has been known as one of the promising materials for water oxidation with the proper valence band edge position located at near 2.4 eV versus reversible hydrogen electrode (RHE).[25] In addition, $BiVO_4$ has many advantages for water oxidation such as appropriate band gap (2.4 eV) for visible light absorption, earth abundance, low cost, and good photostability.[26–28] The effective masses of charge carriers in $BiVO_4$ are also calculated to be much lighter than those of other photoactive materials such as TiO_2 and In_2O_3.[29, 30] The theoretic maximum photocurrent density of $BiVO_4$ is evaluated to be 7.5 mA/cm^2 under standard sunlight and the corresponding solar-to-hydrogen conversion efficiency reaches up to 9.2%.[26] To date, however, practical conversion efficiency of $BiVO_4$ materials is far below than the expected value, because of the excessive electron–hole recombination, slow charge transportation, and poor water oxidation kinetics. Therefore, numerous strategies have been progressed to overcome the drawbacks and limitations for commercial use of $BiVO_4$ in solar water splitting.

Herein, we focus on the strategies to design and fabricate highly efficient $BiVO_4$ photoelectrodes for water oxidation. Various approaches such as morphology control, orientation control, constructing heterostructures, utilizing plasmonic effects, co-catalyst loading, and control of interface band

* These authors contributed equally to this work.

https://doi.org/10.1557/mrc.2018.106 Published online by Cambridge University Press

bending with ferroelectrics are introduced. The most up-to-date techniques, ideas, concepts, and insights to increase the water-splitting performance of the photoanode material are contained in this article that are applicable to other photoelectrodes.

Strategies for highly efficient bismuth vanadate photoanode

The major limiting factors of $BiVO_4$ are (1) significant recombination of electron and holes, (2) poor electrical conductivity, and (3) a slow hole injection rate of water for water oxidation.[31–34] Following strategies are to address one or more limitations of $BiVO_4$ and how these attempts affect the photoelectrochemical performance of $BiVO_4$ is discussed.

Morphology control

Nanostructured materials can provide large surface areas, abundant surface states, and diverse reaction sites compared with the bulk materials.[20] Various attempts have been made to develop novel nanomaterials in recent years.[35–38] However, increasing surface area-to-volume ratio is not always the result in the higher efficiency but gives rise to adverse effects since extra defect sites which can act as recombination sites are also created in the surface.[39] Therefore, fine control to optimize photoelectrochemical property of nanostructured $BiVO_4$ is needed.[40]

Nanostructured $BiVO_4$ can be grown by various methods such as metal–organic decomposition,[31, 41] electrodeposition,[42, 43] chemical vapor deposition,[44] molecular beam epitaxy,[45] and pulsed laser deposition.[46, 47] Jeong et al. prepared high-quality and porous $BiVO_4$ thin film by a pulsed laser deposition method.[48] Low-temperature growth of pulsed laser deposition would bring about a three-dimensional island growth (the Volmer–Weber growth).[49] Three different films with different surface morphologies are synthesized by controlling the deposition temperature as shown in Fig. 1. The substrate was heated to 230, 330, and 430 °C. Microstructures of the $BiVO_4$ grains show significant change with the deposition temperature. As grain size increases with increasing the deposition temperature, surface area decreases. Vertically arranged $BiVO_4$ grains are individually separated in Figs. 1(a) and 1(b), which is deposited at 230 °C. In Figs. 1(c) and 1(d), the film has larger grain size and smooth surface morphology since diffusion of $BiVO_4$ is promoted while deposition at 330 °C. When the film is deposited at 430 °C, grains are coalesced and result in the formation of largest grain and the exposure of underlying F-doped tin oxide glass layer, which is shown in Figs. 1(e) and 1(f). The thickness of the film deposited at 430 °C is about 400 nm. Photocurrent density of the film deposited at 230 °C is substantially enhanced to have 3.0 mA/cm^2 at 1.23 V versus RHE with a hole scavenger where the film deposited at 430 °C exhibited 0.72 mA/cm^2 at 1.23 V.[48] Photogenerated electrons can easily travel to the bottom electrode as depicted in Fig. 1(j), which results in the increase of carrier lifetime of generated holes and thus the rise of the photocurrent density. With the higher process temperature, grains are getting larger, causing the decrease of surface area. In addition, photogenerated electrons cannot reach the bottom electrode and recombine with holes, giving rise to the decrease of photocurrent density.

Kim and Choi demonstrated that electron–hole separation yield of nanoporous $BiVO_4$ can effectively be increased without additional doping when the electrode is composed of nanoparticles (NPs) smaller than its hole diffusion length.[50] Mean particle size was about 76 ± 5 nm, which is smaller than reported hole diffusion length of $BiVO_4$, 100 nm,[51] creating a three-dimensional nanoporous network as shown in Fig. S1. Onset potential of the nanoporous $BiVO_4$ was 0.1 V versus RHE and photocurrent density at 1.23 V was about 4.5 mA/cm^2 with a hole scavenger. Electron–hole separation yield has also been calculated by considering photocurrent density, photon absorption rate, and hole injection yield.[50] Calculated electron–hole separation yield was about 0.90 ± 0.03 at 1.23 V versus RHE, which is noteworthy as a typical value for $BiVO_4$ electrodes is below 0.6 at 1.23 V versus RHE.[28, 31, 32]

Kang et al. fabricated nanodome-structured $BiVO_4$/GaON bilayer for photoanode.[52] $BiVO_4$/GaON forms type I heterojunction. The large energetic barrier of valence band minimum in the GaON would act as a hole mirror and blocks holes to be transferred from $BiVO_4$ to GaON. Subsequently, holes will move to the surface of the $BiVO_4$ layer and participate in oxidizing electrolyte,[44] while electrons recombine at the interface since GaON has large surface defects which can act as recombination sites.[53] To fabricate the $BiVO_4$/GaON nanodome structure, firstly, GaON nanospheres are deposited on the F-doped tin oxide glass substrate, and 50 nm-thick $BiVO_4$ layer is coated on the surface of GaON nanospheres to form a nanodome-structured bilayer photoanode as shown in Fig. S2(e). Nanodome-structured $BiVO_4$/GaON heterostructure (ND-BVO/GaON) has slightly enhanced the light absorption property (75%) compared with the planar $BiVO_4$/GaON heterostructure (P-BVO/GaON, 71% light absorption) and bare $BiVO_4$ photoanodes (62% light absorption). With these two features, type I junction and improved light absorbance, $BiVO_4$/GaON bilayer photoanode has enhanced charge separation and increased photocurrent generation. It is obvious that nanostructured $BiVO_4$ exhibits higher photocurrent density than planar $BiVO_4$ by comparing P-BVO/GaON and ND-BVO/GaON [Fig. S2(a)]. The charge transfer efficiencies ($\eta_{transfer}$) can be calculated by the ratio of the photocurrent densities with H_2O and H_2O_2 electrolytes [Eq. (1)]. Charge transport efficiency ($\eta_{transport}$) is evaluated with the current density in H_2O_2 solution and the total light absorption efficiency (J_{abs}) under AM 1.5G solar spectrum [Eq. (2)].

$$\eta_{transfer} = \frac{J_{H_2O}}{J_{H_2O_2}} \times 100, \quad (1)$$

$$\eta_{transport} = \frac{J_{H_2O_2}}{J_{abs}} \times 100. \quad (2)$$

https://doi.org/10.1557/mrc.2018.106 Published online by Cambridge University Press

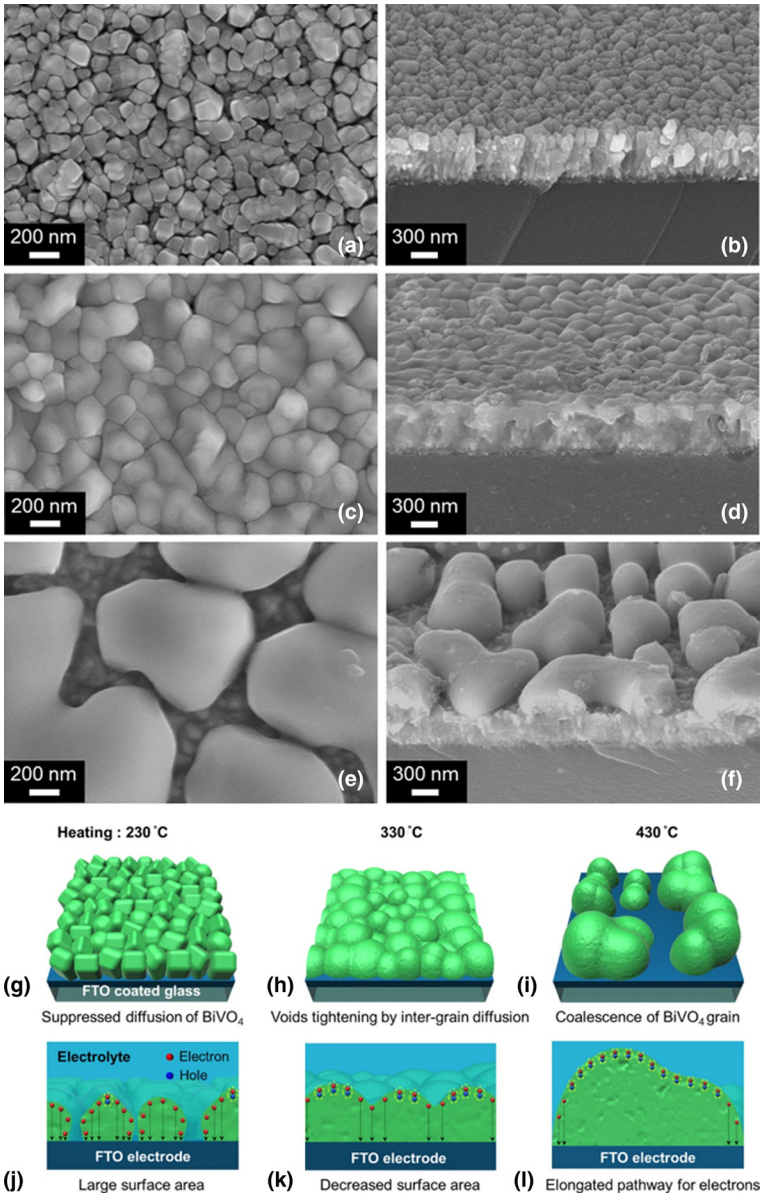


Figure 1. Top and cross-sectional SEM images of BVO films deposited at (a, b) 230 °C, (c, d) 330 °C, and (e, f) 430 °C. Schematic diagram of process temperature effect on (g–i) morphology change and (j–l) its charge collection abilities. Reproduced with permission from Ref. 48. American Chemical Society Publications, 2017.

Figures S2(b) and S2(c) represent the charge transfer efficiency and charge transport efficiency of bare GaON, $BiVO_4$, P-BVO/GaON, and ND-BVO/GaON samples, respectively. Nanostructured $BiVO_4$/GaON has better charge transport and transfer efficiencies since nanostructured $BiVO_4$ provides short electron diffusion pathway.[44, 54] Incident photon-to-current conversion efficiencies (IPCEs) also indicate that ND-BVO/GaON has better value than planar heterostructure. The enhancement of photoanodic properties is attributed to the multiple synergistic effects such as large surface area, enhanced charge separation with type I heterojunction, and larger light absorption properties.

Orientation control

Crystal plane exposed at the interface plays an important role in the photoelectrochemical properties of single-crystal semiconducting photoelectrode.[40, 55, 56] Control of growth orientation and facet can improve the photoconversion efficiency because it affects both the kinetic (e.g., catalytic ability) and thermodynamic factors (e.g., band bending) of the photoelectrode reactions.[40, 57–60]

A few studies on facet engineering to enhance the intrinsic properties of $BiVO_4$ photoelectrodes have been reported. Recently, Han et al. reported that pristine $BiVO_4$ photoanodes with [001]-preferred orientation (p-BVO) were deposited by

https://doi.org/10.1557/mrc.2018.106 Published online by Cambridge University Press

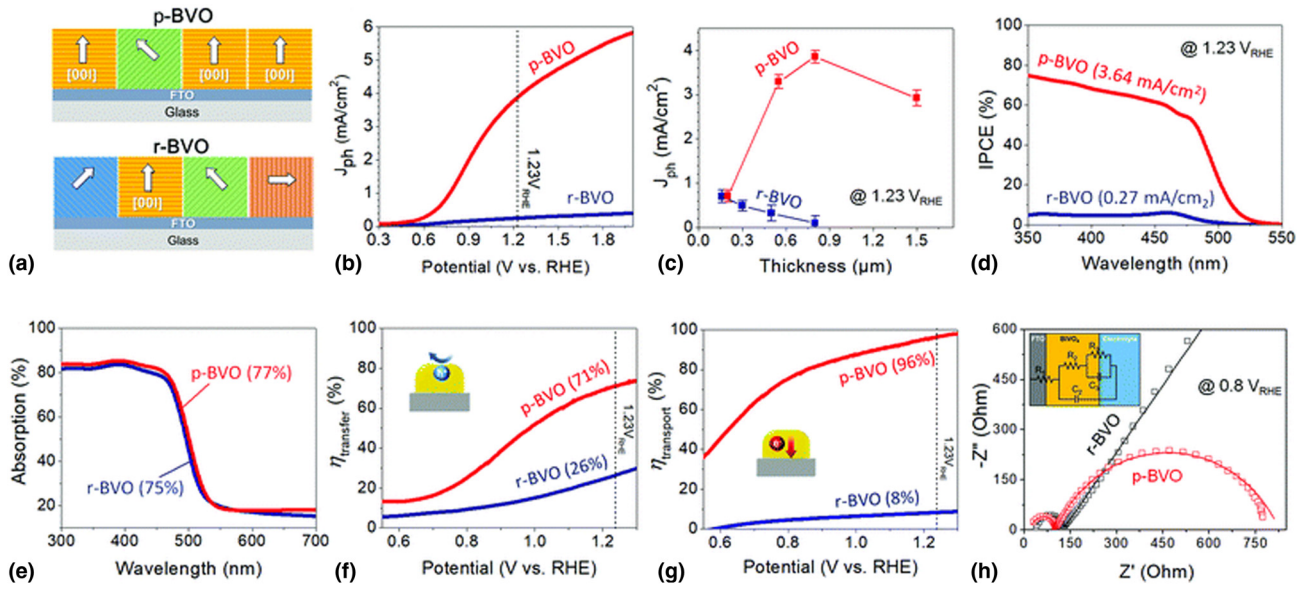


Figure 2. (a) Schematic diagram of the different grain orientation between p-BVO and r-BVO. (b) Photocurrent–potential (*J*–*V*) curves, (c) thickness-dependent photocurrent densities, (d) incident photon-to-current conversion efficiencies (IPCEs) measurement, (e) light absorption, (f) charge transfer efficiencies, (g) charge transport efficiencies, and (h) the results of electrochemical impedance spectroscopy. Reproduced with permission from Ref. 61. Royal Society of Chemistry, 2018.

laser ablation method with a KrF excimer laser.[61] The $BiVO_4$ films composed of rounded-edge columnar grains were ~800 nm thick and about 41% of the grains were the preferred [001] growth orientation (space group: *I*2/*b*, $a = 5.1935$ Å, $b = 5.0898$ Å, $c = 11.6972$ Å, 90.3871°). For observation of orientation effects, they synthesized randomly oriented $BiVO_4$ films (r-BVO) by sol–gel drop-casting method [Fig. 2(a)]. As shown in Fig. 4(b), the photocurrent density of p-BVO photoanodes reached 3.9 mA/cm^2 (at 1.23 V versus RHE), which was ~16 times higher than that of r-BVO photoanodes (0.25 mA/cm^2 at 1.23 V versus RHE). They showed the enhanced charge transport efficiency of p-BVO through the measurements of thickness-dependent $J_{ph,1.23V}$ [Fig. 2(c)]. Unlike r-BVO, the photocurrent density of p-BVO increased with increasing film thickness and remained high even at ~1.5 μm thickness. Improved PEC performance of p-BVO was confirmed by IPCEs [Fig. 2(d)]. The highest IPCE values of p-BVO and r-BVO (at 350 nm) were 74% and 7%. The photocurrent density (J_{ph}) is determined by light absorption expressed in current density (J_{abs}), charge transfer efficiency ($\eta_{transfer}$) at the interface between the photoelectode and electrolyte, and charge transport efficiency ($\eta_{transport}$).[62, 63]

$$J_{ph} = J_{abs} \times \eta_{transfer} \times \eta_{transport}. \quad (3)$$

The preferred [001] orientation growth had little effect on light absorption [Fig. 2(e)]. In contrast, the increased $\eta_{transfer}$ [Fig. 2(f)] and $\eta_{transport}$ [Fig. 2(g)] contributed to significantly improved PEC performance of p-BVO [Fig. 2(d)]. The results of electrochemical impedance spectroscopy (EIS) measurements [Fig. 2(h)] showed smaller bulk and interface resistances of p-BVO, which was the reason of enhanced $\eta_{transfer}$ and $\eta_{transport}$.

Kim et al. prepared (040)-crystal facet $BiVO_4$ [(040)-BVO] photoanodes (space group: *I*2/*a*, $a = 5.195$ Å, $b = 11.701$ Å, $c = 5.092$ Å, $\beta = 90.38°$) by hydrothermal method.[64] For investigating the relationship between the (040)-crystal facet and PEC performance, they compared the photoelectrochemical characteristic of (040)-BVO, $BiVO_4$ seed layer, and $BiVO_4$ plate film. The (040)-BVO photoanodes produced the photocurrent density of 0.94 mA/cm^2, which was higher than that of $BiVO_4$ seed layer (0.1 mA/cm^2) and $BiVO_4$ plate film (0.35 mA/cm^2) at 1.23 V versus RHE under AM 1.5G illumination. They explained that (040)-crystal facet induces photogenerated charge flow and enhances charge transfer and charge separation. IPCE and the absorbed photon-to-current conversion efficiency (APCE) of (040)-BVO photoanodes were 37.5% and 42.1% at 1.23 V versus RHE. Based on the equation of IPCE (%) = charge transport efficiency (η_{trans}) × charge separation efficiency (η_{sep}) × charge transfer efficiency at the solid–liquid junction interface (η_{inter}), these IPCE and APCE results were enhanced by using (040)-crystal planes that cause high light absorption and η_{sep}, considering that interfacial charge transfer efficiency is considered when using co-catalysts.[65–67]

Heterojunction

Due to the broad range absorption of sunlight and enhanced photogenerated electron–hole pair separation with type II

https://doi.org/10.1557/mrc.2018.106 Published online by Cambridge University Press

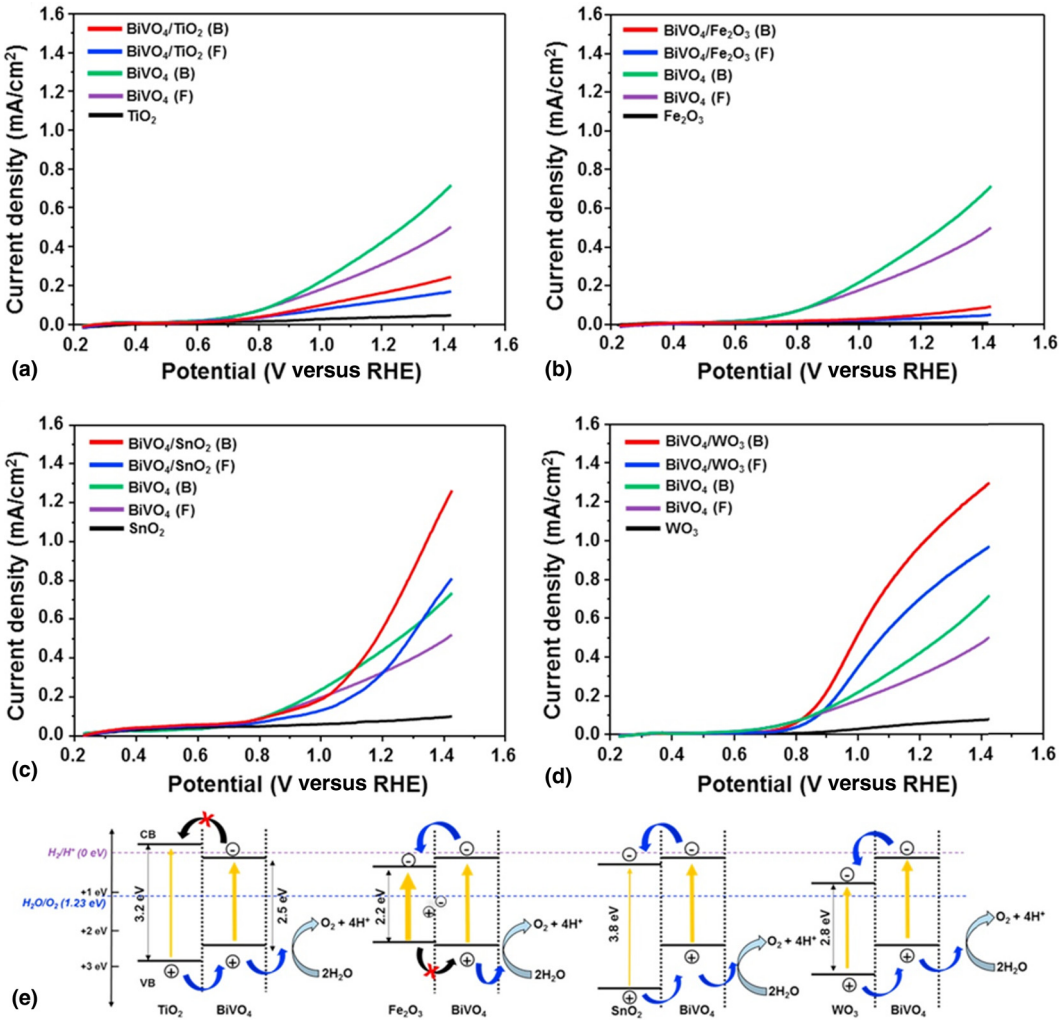


Figure 3. Photocurrent–potential (*J*–*V*) curves of (a) BVO/TiO_2, (b) BVO/Fe_2O_3, (c) BVO/SnO_2, and (d) BVO/WO_3. (e) Illustrations of the band structures of BVO heterojunction photoanodes. Reproduced with permission from Ref. 72. Elsevier, 2016.

band alignment, heterostructures and heterojunctions are reported as promising photoelectrodes.[52] Various combinations have been studied for the formation of type II heterojunctions.[68–70] Among them, $BiVO_4/WO_3$ heterostructure is one of the most attractive combinations.[71]

Since WO_3 is stable in aqueous solution under light illumination and can absorb blue light, WO_3 has been reported as a good photoanode for PECs. However, theoretical solar-to-hydrogen efficiency is limited up to 4.5% with its wide band gap of 2.7 eV. A synergistic enhancement of the photoactivity can be expected when $BiVO_4$ and WO_3 are combined with their merits: good charge transport properties of WO_3 and good optical absorption properties of $BiVO_4$.[71] Hong et al. demonstrated $BiVO_4/WO_3$ heterojunction electrode for the advanced water oxidation property.[71] Energy band diagram of the heterostructure is depicted in Fig. S3(a). $BiVO_3$ and WO_3 construct type II junction; thus, conduction band minimum and valence band maximum of $BiVO_4$ are more negatively located than the conduction band minimum and valence band maximum of WO_3. This condition induces the electron injection from $BiVO_4$ to the conduction band of WO_3 and hole injection from WO_3 to the valence band of $BiVO_4$. Electrons generated in the WO_3 layer and electrons migrated to WO_3 from the $BiVO_4$ layer are collected onto the F-doped tin oxide layer. This facile transfer of electrons would reduce the recombination rate. Holes, on the other hand, are transferred to the $BiVO_4$ layer from WO_3 and migrated to the semiconductor/electrolyte interface to oxidize water. Thus, the heterostructure with type II structure would have enhanced photoactivity and water oxidation property. Photoelectrochemical performance of the $BiVO_4/WO_3$ combined structure is measured as Fig. S3(b). Total thicknesses of the films are 3 μm and the portion of $BiVO_4$ is 20%, 40%, 60%, and 80% in composite 1, 2, 3, and 4, respectively. The inset figure of Fig. S3(b) is the

https://doi.org/10.1557/mrc.2018.106 Published online by Cambridge University Press

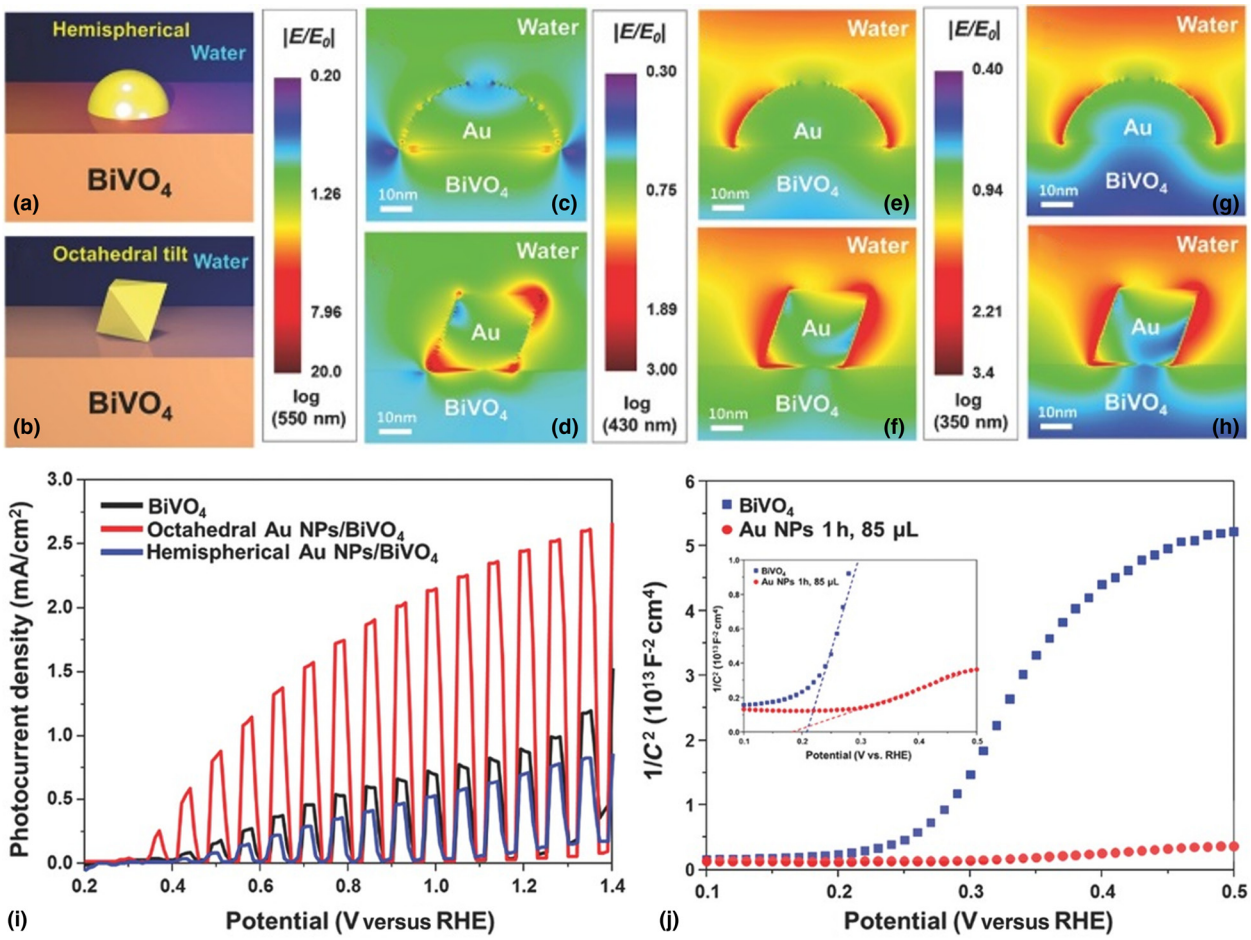


Figure 4. Finite-difference time-domain (FDTD) configurations on BVO. (a) Hemispherical Au NP and (b) octahedra Au NP. Field enhancement for (c) hemispherical Au NP and (d) octahedral Au NP under 550 nm photons. Field enhancement for (e) hemispherical Au NP and (f) octahedral Au NP under 430 nm photons. Field enhancement for (g) hemispherical Au NP and (h) octahedral Au NP under 350 nm photons. (i) Photocurrent–potential (*J*–*V*) curves and (j) Mott–Schottky plot. Reproduced with permission from Ref. 80. WILEY-VCH Verlag GmbH & Co. KgaA, Weinheim, 2017.

magnified view in 0–0.5 V versus Ag/AgCl. The onset potential of WO_3 is about 0.25 V versus Ag/AgCl where onsets of composite films are negatively shifted to 0.05 V versus Ag/AgCl by combining with $BiVO_4$ layer. Photocurrent density is also enhanced with composite 1 compared with bare $BiVO_4$ and bare WO_3. Photogenerated electrons in $BiVO_4$ are migrated to the WO_3 layer with good charge transport characteristics and stimulate the high photoactivity. Thus, fabrication of heterojunction of $BiVO_4/WO_3$ is an efficient method to improve the photoelectrochemical performance for water oxidation.

As shown in Fig. 3, various materials including WO_3 have been tested to combine with $BiVO_4$ for better water oxidation properties.[72] Linear sweep voltammetry curves of various heterostructures are displayed in Figs. 3(a)–3(d). When $BiVO_4$ is combined with TiO_2 and Fe_2O_3, inferior properties are exhibited (Figs. 3(a) and 3(b)]. The electron affinity of $BiVO_4$ is larger than that of TiO_2.[73] Thus, photogenerated electrons in the $BiVO_4$ layer cannot be transferred to TiO_2 as the conduction band minimum of TiO_2 is located higher than that of $BiVO_4$. On the other hand, despite the fact that the conduction band minimum of Fe_2O_3 is lower than that of $BiVO_4$, valence band maximum of Fe_2O_3 is placed slightly higher than that of $BiVO_4$. Holes generated in the Fe_2O_3 layer are blocked to be migrated to the $BiVO_4$ layer and these excessive holes recombine with electrons, leading to the lower water oxidizing property of the heterostructure. Combining with SnO_2 or WO_3 leads to the enhanced water oxidizing performance compared with the bare $BiVO_4$ [Figs. 3(c) and 3(d)]. Both the heterostructures form type II junction, which promotes charge separation and provide conduction pathways. Among these two heterostructures, $BiVO_4/WO_3$ shows superior photocurrent density than $BiVO_4/SnO_2$ since SnO_2 has wide band gap (3.8 eV) where WO_3 has smaller band gap (2.6 eV) compared with SnO_2.

Fabricating nanostructured heterojunction photoanode would have much enhanced property.[72, 74] Porous WO_3 nanorods can be deposited with glancing angle deposition

https://doi.org/10.1557/mrc.2018.106 Published online by Cambridge University Press

method. Pihosh et al. demonstrated a nanostructured $BiVO_4$/WO_3 photoanode deposited on the indium tin oxide underlayer with a photocurrent of 3.2 mA/cm^2 at 1.23 V versus RHE. With a glancing angle deposition of sputtering, WO_3 nanorods are deposited and $BiVO_4$ is deposited on the top of the nanorods.[74] The optimum thickness of WO_3 and $BiVO_4$ is 2.5 μm and 45 nm, respectively. Figure S4 shows the $BiVO_4$/WO_3 heterojunction synthesized by glancing angle deposition (WO_3) and pulsed anodic electrodeposition ($BiVO_4$).[72] $BiVO_4$ nanodots are deposited on the entire surface of WO_3 nanorods. Figures S4(a) and S4(b) indicate that the deposited $BiVO_4$ nanodots are extremely small. X-ray diffraction data shown in Fig. S4(c) reveal that $BiVO_4$/WO_3 heterojunction is fabricated on the F-doped tin oxide substrate. Figures S4(d) and S4(e) designate that the size of the $BiVO_4$ nanodots is about 30 nm. High-resolution images in Figures S4(f) and S4(g) and diffraction patterns of the selected area show that the *d*-spacing of 0.365 and 0.521 nm correspond to the (110) and (001) planes of monoclinic WO_3 nanorods, respectively, and *d*-spacing of 0.238 nm corresponds to the (220) plane of $BiVO_4$. This nanostructured heterojunction performed the enhancement of photocurrent density at 1.23 V versus RHE. The photocurrent density of nanostructured $BiVO_4$/WO_3 is about 4.55 mA/cm^2, where the nanostructured WO_3 without $BiVO_4$ is about 2.1 mA/cm^2. This suggests that the nanostructured heterojunction has all the advantages of $BiVO_4$, WO_3, and nanostructure.[72]

Fabricating *p*–*n* junction is also an effective way to produce type II band alignment. Chang et al. demonstrated the synergetic enhancement of surface reaction and charge separation by introducing *p*-type Co_3O_4 nanodots on *n*-type $BiVO_4$, forming a *p*–*n* junction with an internal electric field to assist the charge separation.[75] As displayed in Fig. S5, photogenerated electrons in $BiVO_4$ are prohibited from transferring to Co_3O_4, whereas holes on the valence band of $BiVO_4$ can be migrated to that of Co_3O_4.[76] Consequently, the separation of photogenerated electron–hole pairs is substantially improved. In addition, surface reaction can be boosted since Co_3O_4 lowers the overpotential required for water oxidation.[77, 78] Photocurrent of Co_3O_4/$BiVO_4$ *p*–*n* junction heterostructure shows 2.71 mA/cm^2 at 1.23 V versus RHE for water splitting without a hole scavenger and 6 mA/cm^2 at 1.23 V versus RHE with a hole scavenger. Thus, fabricating heterostructure with the materials that can form type II junction is one of the fascinating strategies for superior water oxidation photoelectrode.

Combination with plasmonic nanoparticles

Plasmonic metal NPs have been actively studied for solar water splitting due to their ability to overcome many limitations of photoanodes. Especially, gold (Au) and silver (Ag) NPs are mainly used for solar water splitting because of their chemical stability, Schottky junction formation, and localized surface plasmon resonance (LSPR) in the visible spectral region. The formation of Schottky junction improves charge transfer, modifies the electronic band structure, and promotes charge separation.[79] LSPR also has several advantages in improving solar water splitting.[80–84] First, the plasmon-resonant energy transfer (PRET) effect can produce field-enhanced electron–hole pair near the semiconductor surface. Second, plasmon-induced direct electron transfer (DET) contributes to the creation of additional charge carriers through injecting the hot electrons generated by surface plasmons into the conduction band of the semiconductor. Third, resonant photon scattering of metal NPs greatly increases the average photon path length. Au and Ag NPs can reduce the charge recombination rate because of strong surface plasmon resonance and confinement of the light near their surface.[81–83, 85–88]

There are several studies on $BiVO_4$ with geometrically controlled plasmonic Au or Ag NPs. Zhang *et. al* investigated $BiVO_4$ films with Au NPs size-dependent plasmonic effect.[81] They prepared photoanodes by drop-casting Au NPs with the diameters of 10, 20, 30, 40, 60, and 80 nm onto the $BiVO_4$ films. All of the $BiVO_4$ photoanodes with Au NPs showed higher photocurrent densities than the $BiVO_4$ photoanodes without Au NPs, and 20 and 30 nm Au NPs on $BiVO_4$ photoanodes obtained highest photocurrent densities. In order to understand the PRET effect with different sizes of Au NPs, they simulated the electric field distribution based on finite-different time-domain (FDTD) method. The simulation showed that with increasing the size of Au NP, the volume of electric field enhancement also increased. The photogenerated holes with enhanced electric field are able to diffuse the $BiVO_4$ surface. It means that the photogenerated charge carrier can be separated in the space charge layer. They also observed the enhancement factor that varied with incident light wavelength. The electric field enhancement reached a maximum value at around 580 nm for all of the Au NPs. This enhanced light absorption and localized light absorption on the $BiVO_4$ surface can help the readily separated charge carrier generation in the space charge layer. But for the experiment, Au NPs with larger diameter than 40 nm reduced the PRET effect because of the red shift of the plasmonic absorption resonance. They confirmed that, unlike the PRET effect, the effect of scattering and hot electron injection were weak for the $BiVO_4$ photoanodes with Au NPs. They also performed the angle-dependent PRET effect, and they observed strong PRET effect with larger off-normal irradiation angles.

Recently, $BiVO_4$ photoanodes with shape-controlled Au NPs also have been studied. Hemispherical and octahedral Au NPs have been utilized to observe the shape-dependent plasmonic effect.[80] $BiVO_4$ films were deposited by pulsed anodic electrodeposition method with post-annealing process for crystalline monoclinic phase. Octahedral Au NPs were synthesized by seed-mediated growth method, and then they attached them on prepared $BiVO_4$. Hemisphere Au-deposited $BiVO_4$ was deposited by electron beam evaporator. In order to observe the Au NP shape-dependent field enhancement, they performed FDTD simulation [Figs. 4(a)–4(h)]. $BiVO_4$

https://doi.org/10.1557/mrc.2018.106 Published online by Cambridge University Press

films with octahedral NPs showed higher intensified LSPR electric fields (LSPR-EFs) than the hemisphere Au NPs due to their well-defined edges and sharp vertices.[83, 89–91] The sharp vertices of plasmonic Au NPs reduce the restoring force of electron oscillation, which can enhance the charge separation in the semiconductor.[92, 93] The photocurrent density of $BiVO_4$ photoanodes with octahedral Au NPs reached 2.4 mA/cm^2 at the 1.23 V versus RHE, which was three times higher than that of bare $BiVO_4$ photoanodes [Fig. 4(i)]. This is due to their high absorption, enhanced charge generation, and improved charge separation by DET and PRET, which are LSPR-induced effects.

Jeong et al. studied about plasmonic Ag NPs with $BiVO_4$ photoanodes.[94] Fully solution-deposited Ag-impregnated nanocomposite $BiVO_4$ (Ag-BVO) photoanodes were studied for solar water splitting. The simulation showed that impregnated Ag NPs in $BiVO_4$ maximized the use of the LSPR-induced enhancement effect. The photocurrent density of Ag-BVO photoanodes was 3.3 times higher than that of pristine $BiVO_4$ photoanode at 0.4 V versus RHE. They explained it by the mechanism of LSPR-induced enhancement. When they illuminated the visible light and ultraviolet light, both of $BiVO_4$ and Ag NPs absorbed the light and the Ag NPs generated the localized electric field by LSPR. The steep increase and the improved saturated current density are attributed to the carrier concentration increase by the charge carrier generation. In order to characterize the carrier excitation in Ag-BVO, they measured photoluminescence (PL). The results showed that the PL intensities increased with increasing concentration of Ag NPs. It is because the intensities of PL are proportional to the amount of carrier recombination. Therefore, the results of PL imply that an increase of carrier concentration is the result of the LSPR-induced effects. They also analyzed the EIS for observing the improved charge carrier separation mechanisms induced by Schottky junction formation.[82, 95–101]

Co-catalyst loading

The biggest limitations of $BiVO_4$ are poor surface catalytic reaction for water oxidation and slow kinetics for oxygen evolution.[23, 32, 102] Thus, various types of electrocatalysts, such as cobalt phosphate (Co-Pi), NiOOH, FeOOH, and CoO_x are commonly deposited on the top of the $BiVO_4$ electrode to improve the charge transfer efficiency.[50, 52] The most commonly used catalyst to improve water oxidation kinetics is Co-Pi catalyst developed by Kanan and Nocera.[18] Accumulation of holes in the surface of the $BiVO_4$ results in the recombination of electrons and holes. Co-Pi blocks the accumulation of holes in the interface since Co-Pi-catalyzed surface has faster water oxidizing kinetics and lower overpotential is required. Co-Pi has been reported to improve the performance of Fe_2O_3,[97, 103, 104] WO_3,[98] and other photoanode materials under neutral pH conditions.[105–107] Certainly, Co-Pi is also effective for the performance of $BiVO_4$ photoelectrode.[32] For photoelectrochemical water oxidation, the thickness of the Co-Pi catalyst layer is sensitive; thus, fine tuning of the thickness is indeed needed to optimize the performance.[108, 109]

Abdi and van de Krol reported 1.7 mA/cm^2 at 1.23 V versus RHE without a hole scavenger for Co-Pi-catalyzed $BiVO_4$ photoanodes with a thickness of 100 nm prepared by spray pyrolysis.[32] As shown in Fig. S6(a), the photocurrent density of bare $BiVO_4$ is 0.6 mA/cm^2, whereas Co-Pi-catalyzed $BiVO_4$ has much enhanced value. Photocurrent transient measurements are depicted in Fig. S6(b). When the sample absorbs light, photogenerated holes travel to the electrode surface and accumulate because of the poor oxygen evolution reaction kinetics.[110] Thus, a sharp anodic current spike is appeared and the current density decays as the accumulation process reaches the equilibrium.[111] When the light is switched off, the accumulated holes recombine with electrons in the conduction band, causing the cathodic response of the black line in Fig. S6(b). With the Co-Pi catalyst layer, hole injection rate of water is enhanced, leading to the low electron–hole recombination. Consequently, photocurrent for water oxidation without a hole scavenger is improved to the level of photocurrent for H_2O_2 oxidation, indicating that oxygen evolution kinetics are improved. Figure S6(c) shows the photocurrent density as a function of the thickness of Co-Pi on $BiVO_4$ photoelectrode. Co-Pi thickness of 30 nm has the highest photocurrent density compared with other thicknesses. Thus, the optimum thickness of Co-Pi is about 30 nm. This is because the Co-Pi layer is not wholly covering the $BiVO_4$ when the thickness is thinner than 30 nm, while hole transport through the Co-Pi layer may become worse for thicker films.[32]

Loading NiO on the surface of $BiVO_4$ is one of the feasible approaches to enhance water-splitting performance. Since NiO is a *p*-type oxide, a buried *p*–*n* junction can be easily created at the photoanode surface with NiO surface layer. The photogenerated holes will be extracted from $BiVO_4$ photoanode and stored in the surface *p*-type NiO with a prolonged life time. In addition, *p*-type NiO would turn into hydroxyl-ion permeable NiOOH on the photoanode surface during water oxidation process. Zhong et al. demonstrated dual catalyzed $BiVO_4$ NPs with CoO_x and NiO for photoelectrochemical water oxidation.[112] The NiOOH layer is formed at the surface as shown in Fig. 5. The optimal thickness of NiO layer is 6 nm and NiO/CoO_x/$BiVO_4$ photoanode reaches 3.5 mA/cm^2 at 1.23 V versus RHE, which is a twofold increased value compared with that of the CoO_x/$BiVO_4$ photoanode.[112] Kim and Choi assembled thin NiOOH and FeOOH layers on the nanoporous $BiVO_4$ surface.[50] Photocurrent of the NiOOH/$BiVO_4$ and FeOOH/$BiVO_4$ photoanodes was significantly higher than the bare $BiVO_4$ photoanode. Thus, depositing NiO on the surface which will naturally turn into NiOOH can be also applied to other semiconducting photoelectrode toward highly efficient solar fuel generation.

Control of interfacial band bending with ferroelectrics

Ferroelectric materials have ferroelectric self-polarization field and high built-in potential that can improve the drift and

https://doi.org/10.1557/mrc.2018.106 Published online by Cambridge University Press

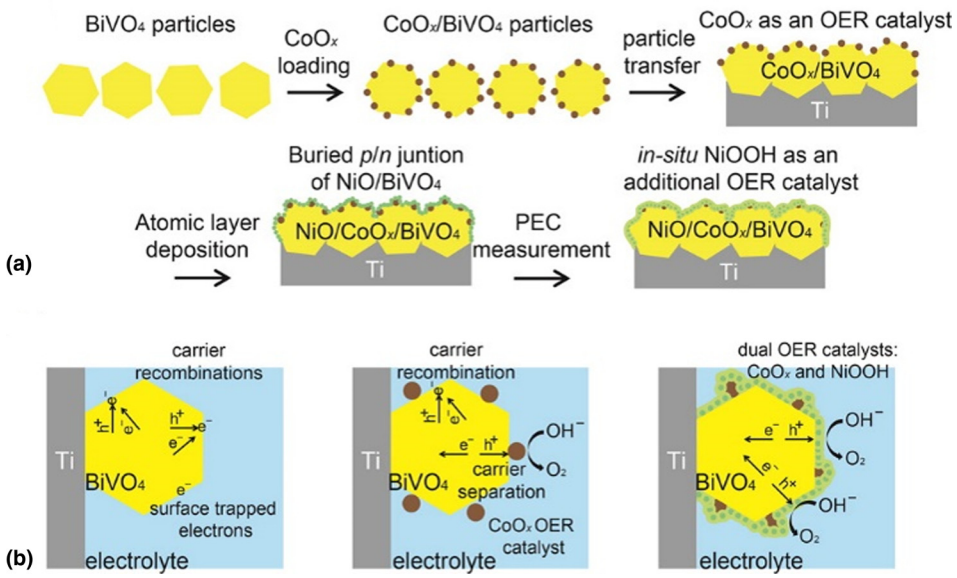


Figure 5. (a) Fabrication process of the NiOOH/NiO/CoO_x/BVO/Ti photoanodes and (b) schematic diagram of proposed recombination/separation process. Reproduced with permission from Ref. 112. American Chemical Society Publications, 2015.

separation of photogenerated carriers.[10, 113] Recently, $BiFeO_3$ (BFO) perovskite ferroelectric material is actively studied for enhancing the solar water splitting. Because it possesses high Curie temperature ($T_c = 1000$ K), suitable bandgap energy (~2.1 eV) is required to absorb the visible light, intrinsic polarization field, and chemical stability.[113–116] Until recently, there have been a few papers that have greatly enhanced the results of BFO photoanodes-based PEC because of their high

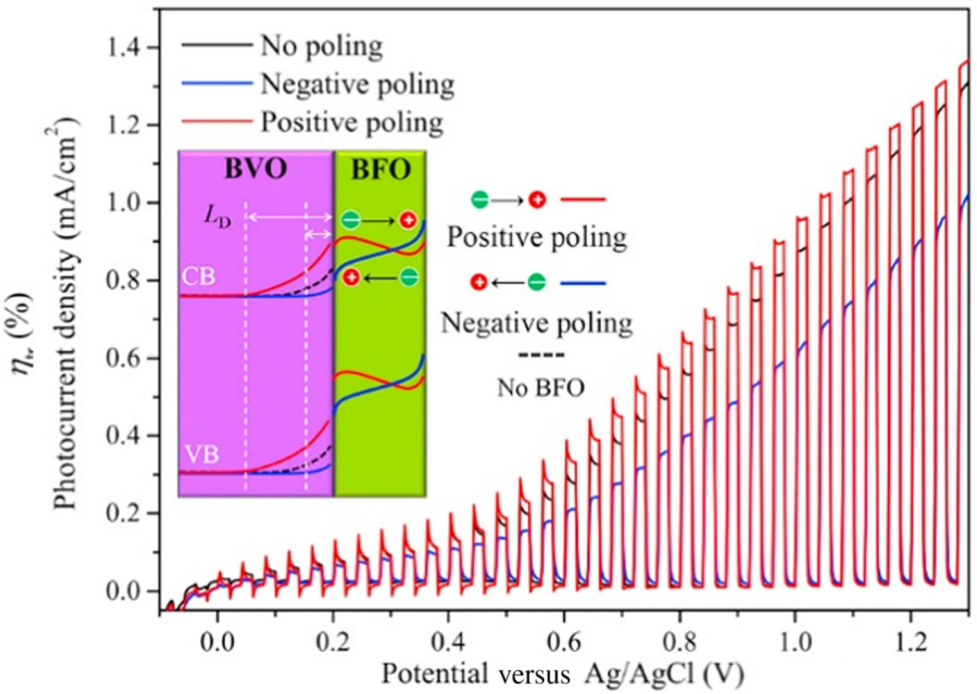


Figure 6. Chopped photocurrent–potential (*J*–*V*) curves and schematic mechanism of the BVO/BFO photoanode. Reproduced with permission from Ref. 113. Elsevier, 2017.

https://doi.org/10.1557/mrc.2018.106 Published online by Cambridge University Press

Table I. Review on the strategies and photoelectrochemical performance of references.

Strategy	Current density (mA/cm^2) at 1.23 V versus RHE	Hole scavenger	Authors	Ref.
Morphology control	3.0	0.5 M Na_2SO_3	Jeong et al.	[48]
Morphology control	4.5	0.1 M Na_2SO_3	Kim and Choi	[50]
Morphology control	0.37	H_2O_2	Kang et al.	[52]
Orientation control	3.9	H_2O_2	Han et al.	[61]
Orientation control	0.94	H_2O_2	Kim et al.	[64]
Heterojunction	1.74	0.05 M methanol	Hong et al.	[71]
Heterojunction	4.55	0.1 M Na_2SO_3	Lee et al.	[72]
Heterojunction	3.2	–	Pihosh et al.	[74]
Heterojunction	2.71	1 M Na_2SO_3	Chang et al.	[75]
Combination with plasmonic NPs	2.4	1 M Na_2O_3	Lee et al.	[80]
Co-catalyst loading	1.7	0.5 M H_2O_2	Abdi and van de Krol	[32]
Co-catalyst loading	3.5	1 M Na_2O_3	Zhong et al.	[112]

dielectric constant, low visible light absorbance, and their insulating nature.

Xie et al. reported that the BFO passivated $BiVO_4$ (BVO/BFO) photoanodes showed enhanced photoelectrochemical properties.[113] They synthesized $BiVO_4$ thin films by dipping method with post-annealing process. After the preparation of the $BiVO_4$ films, they fabricated BVO/BFO thin films by chemical solution deposition method. The photocurrent density of BVO/BFO photoanode was 0.63 mA/cm^2 at 0.6 V versus RHE, which is 4.4 and 1.24 times higher than that of bare

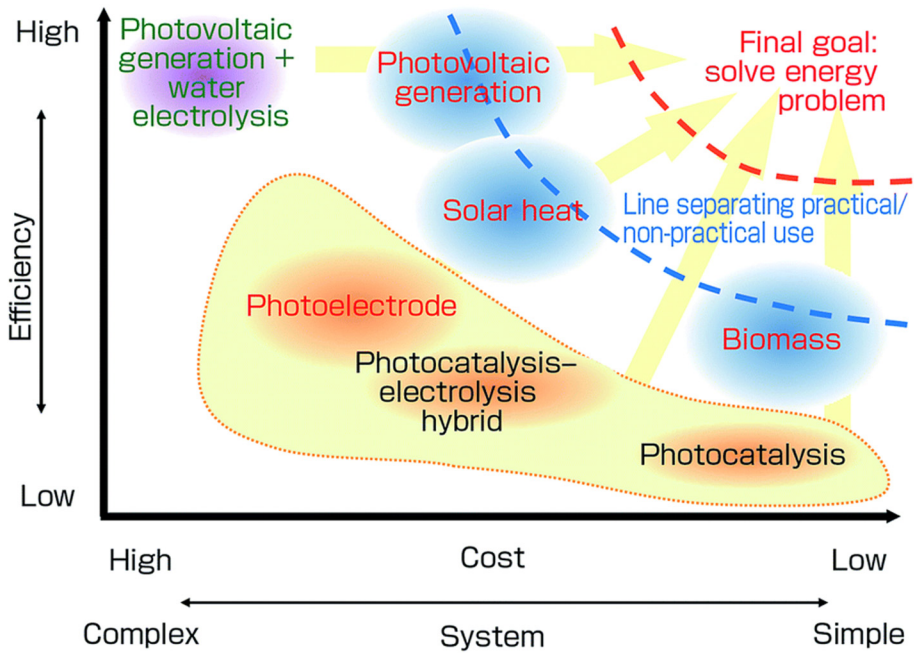


Figure 7. Technologic map showing various approaches to solar energy conversion. Reproduced with permission from Ref. 120. Royal Society of Chemistry, 2017.

https://doi.org/10.1557/mrc.2018.106 Published online by Cambridge University Press

BVO and BVO/Co-Pi photoanodes. The onset voltage of the BVO/BFO photoanode was 0.03 V versus RHE, which is ~0.40 and ~0.22 V lower than that of the BVO and BVO/Co-Pi photoanodes. It means that the BFO passivation layer accelerates the OER kinetics in photoanode. In order to confirm the ferroelectric polarization effect, they measured PEC performance after poling the BVO/BFO photoanode (Fig. 6). The photocurrent density of the BVO/BFO with positive poling increased by 19%. In contrast, the photocurrent density with negative poling decreased to be ~75.6%, which means that the band bending is downward at the surface and the charge separation efficiency is limited. These results imply the exist of the self-polarization direction of the BFO layer. They also showed greatly enhanced APCE value of 21.2% at the wavelength of 360 nm compared with 10.0% and 15% of bare BVO and BVO/Co-Pi photoanodes. It means that the BFO passivation layer can suppress the charge recombination. The charge transfer and separation efficiency were also enhanced and the long-term stability was better than BVO/Co-Pi photoanode. They explained that the self-polarization of BFO and the type II heterojunction formed by contacting the BVO with BFO can result in the suppressed charge recombination and improved charge transfer/surface OER reaction. The self-polarization in BFO can be caused by strain, oxygen vacancies, and so on, and the effect of self-polarization becomes more important with decreasing the BFO thickness.[117] This means that the thin passivation BFO layer can play a critical role in the formation of a high self-polarization.

Summary and outlook

In summary, we have reviewed the strategies to enhance the water oxidizing properties of $BiVO_4$ for a photoanode in a PEC. Many attempts have been made to improve the performance of $BiVO_4$ such as fabricating nanostructured $BiVO_4$, controlling reacting facet, stacking with other materials, utilizing plasmonic effects, loading co-catalyst, and controlling the interfacial band bending with ferroelectrics as shown in Table I. However, the practical conversion efficiency attained with the $BiVO_4$-based photoelectrode is still below what expected owing to some drawbacks such as low electron–hole separation yield and slow kinetics for water oxidation. Thus, theoretical and experimental studies to further enhance the property of $BiVO_4$ are highly desired.

The US Department of Energy has set the technical target of the solar-to-hydrogen energy conversion efficiency of the photoelectrode system as 20% for 2020.[118] Sayama and Miseki summarized the cost and efficiency of various solar energy conversion systems in the schematic as shown in Fig. 7.[119,120] To date, photovoltaic-assisted electrolysis system shows superior efficiency than photoelectrode water-splitting system. However, this system is too expensive to be cost-competitive. Therefore, the development of photoelectrode solar water-splitting system is required. The strategies, discussion, and insights contained in this article provide a good understanding for current state and development of $BiVO_4$. It is expected that, by combining one or several strategies, the solar-to-hydrogen conversion efficiency of $BiVO_4$-based photoelectrode can be stimulated to a suitable level for practical solar water splitting.

Supplementary material

The supplementary material for this article can be found at https://doi.org/10.1557/mrc.2018.106

Acknowledgments

This work was financially supported by the Future Material Discovery Program (NRF-2016M3D1A1027666) and the Basic Science Research Program (NRF-2017R1A2B3009135) through the National Research Foundation of Korea.

References

1. A. Fujishima and K. Honda: Electrochemical photolysis of water at a semiconductor electrode. *Nature* **238**, 37 (1972).
2. J.R. Bolton: Solar photoproduction of hydrogen: a review. *Sol. Energy* **57**, 37 (1996).
3. S.U.M. Khan and J. Akikusa: Photoelectrochemical splitting of water at nanocrystalline n-Fe_2O_3 thin-film electrodes. *J. Phys. Chem. B* **103**, 7184 (1999).
4. S.U.M. Khan: Stability and photoresponse of nanocrystalline n-TiO_2 and n-TiO_2/Mn_2O_3 thin film electrodes during water splitting reactions. *J. Electrochem. Soc.* **145**, 89 (1998).
5. J. Akikusa and S.U.M. Khan: Photoelectrolysis of water to hydrogen in p-SiC/Pt and p-SiC/n-TiO_2 cells. *Int. J. Hydrogen Energy* **27**, 863 (2002).
6. O. Khaselev and J.A. Turner: A monolithic photovoltaic-photoelectrochemical device for hydrogen production via water splitting. *Science* **280**, 425 (1998).
7. S. Licht, B. Wang, S. Mukerji, T. Soga, M. Umeno, and H. Tributsch: Efficient solar water splitting, exemplified by RuO_2-catalyzed AlGaAs/Si photoelectrolysis. *J. Phys. Chem. B* **104**, 8920 (2000).
8. S.U.M. Khan, M. Al-Shahry, and W.B. Ingler: Efficient photochemical water splitting by a chemically modified n-TiO_2. *Science* **297**, 2243 (2002).
9. J. Song, J. Cha, M.G. Lee, H.W. Jeong, S. Seo, J.A. Yoo, T.L. Kim, J. Lee, H. No, D.H. Kim, S.Y. Jeong, H. An, B.H. Lee, C.W. Bark, H. Park, H. W. Jang, and S. Lee: Template-engineered epitaxial $BiVO_4$ photoanodes for efficient solar water splitting. *J. Mater. Chem. A* **5**, 18831 (2017).
10. J. Song, T.L. Kim, J. Lee, S.Y. Cho, J. Cha, S.Y. Jeong, H. An, W.S. Kim, Y.-S. Jung, J. Park, G.Y. Jung, D.-Y. Kim, J.Y. Jo, S.D. Bu, H.W. Jang, and S. Lee: Domain-engineered $BiFeO_3$ thin-film photoanodes for highly enhanced ferroelectric solar water splitting. *Nano Res.* **11**, 642 (2018).
11. W. Wang, M.O. Tadé, and Z. Shao: Research progress of perovskite materials in photocatalysis- and photovoltaics-related energy conversion and environmental treatment. *Chem. Soc. Rev.* **44**, 5371 (2015).
12. Z.W. Seh, J. Kibsgaard, C.F. Dickens, I. Chorkendorff, J.K. Nørskov, and T.F. Jaramillo: Combining theory and experiment in electrocatalysis: Insights into materials design. *Science* **355**, eaad4998 (2017).
13. S. Dunn: Hydrogen futures: toward a sustainable energy system. *Int. J. Hydrogen Energy* **27**, 235 (2002).
14. J.D. Holladay, J. Hu, D.L. King, and Y. Wang: An overview of hydrogen production technologies. *Catal. Today* **139**, 244 (2009).
15. J.R. Rostrup-Nielsen and T. Rostrup-Nielsen: Large-scale hydrogen production. *Cattech* **6**, 150 (2002).
16. K.C. Kwon, S. Choi, K. Hong, D.M. Andoshe, J.M. Suh, C. Kim, K. S. Choi, J.H. Oh, S.Y. Kim, and H.W. Jang: Tungsten disulfide thin film/p-type Si heterojunction photocathode for efficient photochemical hydrogen production. *MRS Commun.* **7**, 272 (2017).
17. N.S. Lewis and D.G. Nocera: Powering the planet: chemical challenges in solar energy utilization. *Proc. Natl. Acad. Sci.* **103**, 15729 (2006).
18. M.W. Kanan and D.G. Nocera: In situ formation of an oxygen-evolving catalyst in neutral water containing phosphate and Co^{2+}. *Science* **321**, 1072 (2008).

https://doi.org/10.1557/mrc.2018.106 Published online by Cambridge University Press

19. M.A. Henderson: A surface science perspective on TiO_2 photocatalysis. *Surf. Sci. Rep.* **66**, 185 (2011).
20. H. Tong, S. Ouyang, Y. Bi, N. Umezawa, M. Oshikiri, and J.H. Ye: Nano-photocatalytic materials: possibilities and challenges. *Adv. Mater.* **24**, 229 (2012).
21. H. Zhou, Y. Qu, T. Zeid, and X. Duan: Towards highly efficient photocatalysts using semiconductor nanoarchitectures. *Energy Environ. Sci.* **5**, 6732 (2012).
22. Y. Ma, X. Wang, Y. Jia, X. Chen, H. Han, and C. Li: Titanium dioxide-based nanomaterials for photocatalytic fuel generations. *Chem. Rev.* **114**, 9987 (2014).
23. Y. Park, K.J. McDonald, and K.-S. Choi: Progress in bismuth vanadate photoanodes for use in solar water oxidation. *Chem. Soc. Rev.* **42**, 2321 (2013).
24. Z. Zou, J. Ye, K. Sayama, and H. Arakawa: Direct splitting of water under visible light irradiation with an oxide semiconductor photocatalyst. *Nature* **414**, 625 (2001).
25. B. Xie, H. Zhang, P. Cai, R. Qiu, and Y. Xiong: Simultaneous photocatalytic reduction of Cr(VI) and oxidation of phenol over monoclinic $BiVO_4$ under visible light irradiation. *Chemosphere* **63**, 956 (2006).
26. M.S. Prévot and K. Sivula: Photoelectrochemical tandem cells for solar water splitting. *J. Phys. Chem. C* **117**, 17879 (2013).
27. P. Bornoz, F.F. Abdi, S.D. Tilley, B. Dam, R. Van De Krol, M. Graetzel, and K. Sivula: A bismuth vanadate-cuprous oxide tandem cell for overall solar water splitting. *J. Phys. Chem. C* **118**, 16959 (2014).
28. F.F. Abdi, L. Han, A.H.M. Smets, M. Zeman, B. Dam, and R. van de Krol: Efficient solar water splitting by enhanced charge separation in a bismuth vanadate-silicon tandem photoelectrode. *Nat. Commun.* **4**, 2195 (2013).
29. Z. Zhao, Z. Li, and Z. Zou: Electronic structure and optical properties of monoclinic clinobisvanite $BiVO_4$. *Phys. Chem. Chem. Phys.* **13**, 4746 (2011).
30. A. Walsh, Y. Yan, M.N. Huda, M.M. Al-Jassim, and S.-H.H. Wei: Band edge electronic structure of $BiVO_4$: elucidating the role of the Bi s and V d Orbitals. *Chem. Mater.* **21**, 547 (2009).
31. D.K. Zhong, S. Choi, and D.R. Gamelin: Near-complete suppression of surface recombination in solar photoelectrolysis by "co-Pi" catalyst-modified W:$BiVO_4$. *J. Am. Chem. Soc.* **133**, 18370 (2011).
32. F.F. Abdi and R. van de Krol: Nature and light dependence of bulk recombination in Co-Pi-catalyzed $BiVO_4$ photoanodes. *J. Phys. Chem. C* **116**, 9398 (2012).
33. S.P. Berglund, A.J.E. Rettie, S. Hoang, and C.B. Mullins: Incorporation of Mo and W into nanostructured $BiVO_4$ films for efficient photoelectrochemical water oxidation. *Phys. Chem. Chem. Phys.* **14**, 7065 (2012).
34. J. Su, L. Guo, N. Bao, and C.A. Grimes: Nanostructured WO_3/$BiVO_4$ heterojunction films for efficient photoelectrochemical water splitting. *Nano Lett.* **11**, 1928 (2011).
35. P.V. Kamat: Meeting the clean energy demand: nanostructure architectures for solar energy conversion. *J. Phys. Chem. C* **111**, 2834 (2007).
36. D. Chen and J. Ye: $SrSnO_3$ nanostructures: synthesis, characterization, and photocatalytic properties. *Chem. Mater.* **19**, 4585 (2007).
37. H. Zeng, W. Cai, Y. Li, J. Hu, and P. Liu: Composition/structural evolution and optical properties of ZnO/Zn nanoparticles by laser ablation in liquid media. *J. Phys. Chem. B* **109**, 18260 (2005).
38. X. Chen and S.S. Mao: Titanium dioxide nanomaterials: synthesis, properties, modifications and applications. *Chem. Rev.* **107**, 2891 (2007).
39. S.P. Berglund, D.W. Flaherty, N.T. Hahn, A.J. Bard, and C.B. Mullins: Photoelectrochemical oxidation of water using nanostructured $BiVO_4$ films. *J. Phys. Chem. C* **115**, 3794 (2011).
40. K.S. Choi: Shape effect and shape control of polycrystalline semiconductor electrodes for use in photoelectrochemical cells. *J. Phys. Chem. Lett.* **1**, 2244 (2010).
41. Y.S. Chen, J.S. Manser, and P.V. Kamat: All solution-processed lead halide perovskite-$BiVO_4$ tandem assembly for photolytic solar fuels production. *J. Am. Chem. Soc.* **137**, 974 (2015).
42. J.A. Seabold and K.S. Choi: Efficient and stable photo-oxidation of water by a bismuth vanadate photoanode coupled with an iron oxyhydroxide oxygen evolution catalyst. *J. Am. Chem. Soc.* **134**, 2186 (2012).
43. S. Xiao, H. Chen, Z. Yang, X. Long, Z. Wang, Z. Zhu, Y. Qu, and S. Yang: Origin of the different photoelectrochemical performance of mesoporous $BiVO_4$ photoanodes between the $BiVO_4$ and the FTO side illumination. *J. Phys. Chem. C* **119**, 23350 (2015).
44. E. Alarcón-Lladó, L. Chen, M. Hettick, N. Mashouf, Y. Lin, A. Javey, and J.W. Ager: $BiVO_4$ thin film photoanodes grown by chemical vapor deposition. *Phys. Chem. Chem. Phys.* **16**, 1651 (2014).
45. S. Stoughton, M. Showak, Q. Mao, P. Koirala, D.A. Hillsberry, S. Sallis, L.F. Kourkoutis, K. Nguyen, L.F.J. Piper, D.A. Tenne, N.J. Podraza, D. A. Muller, C. Adamo, and D.G. Schlom: Adsorption-controlled growth of $BiVO_4$ by molecular-beam epitaxy. *APL Mater.* **1**, 42112 (2013).
46. A.J.E. Rettie, S. Mozaffari, M.D. McDaniel, K.N. Pearson, J.G. Ekerdt, J. T. Markert, and C.B. Mullins: Pulsed laser deposition of epitaxial and polycrystalline bismuth vanadate thin films. *J. Phys. Chem. C* **118**, 26543 (2014).
47. C.N. Van, W.S. Chang, J.W. Chen, K.A. Tsai, W.Y. Tzeng, Y.C. Lin, H. H. Kuo, H.J. Liu, K. Der Chang, W.C. Chou, C.L. Wu, Y.C. Chen, C. W. Luo, Y.J. Hsu, and Y.H. Chu: Heteroepitaxial approach to explore charge dynamics across Au/$BiVO_4$ interface for photoactivity enhancement. *Nano Energy* **15**, 625 (2015).
48. S.Y. Jeong, K.S. Choi, H.M. Shin, T.L. Kim, J. Song, S. Yoon, H.W. Jang, M.H. Yoon, C. Jeon, J. Lee, and S. Lee: Enhanced photocatalytic performance depending on morphology of bismuth vanadate thin film synthesized by pulsed laser deposition. *ACS Appl. Mater. Interfaces* **9**, 505 (2017).
49. M.N.R. Ashfold, F. Claeyssens, G.M. Fuge, and S.J. Henley: Pulsed laser ablation and deposition of thin films. *Chem. Soc. Rev.* **33**, 23 (2004).
50. T.W. Kim and K.-S. Choi: Nanoporous $BiVO_4$ photoanodes with dual-layer oxygen evolution catalysts for solar water splitting. *Science* **343**, 990 (2014).
51. A.J.E. Rettie, H.C. Lee, L.G. Marshall, J.F. Lin, C. Capan, J. Lindemuth, J. S. McCloy, J. Zhou, A.J. Bard, and C.B. Mullins: Combined charge carrier transport and photoelectrochemical characterization of $BiVO_4$ single crystals: intrinsic behavior of a complex metal oxide. *J. Am. Chem. Soc.* **135**, 11389 (2013).
52. B.K. Kang, G.S. Han, J.H. Baek, D.G. Lee, Y.H. Song, S. Bin Kwon, I. S. Cho, H.S. Jung, and D.H. Yoon: Nanodome structured $BiVO_4$/GaO_xN_{1-x} photoanode for solar water oxidation. *Adv. Mater. Interfaces* **4**, 1700323 (2017).
53. N. Iqbal, I. Khan, Z.H. Yamani, and A. Qurashi: Sonochemical assisted solvothermal synthesis of gallium oxynitride nanosheets and their solar-driven photoelectrochemical water-splitting applications. *Sci. Rep.* **6**, 1 (2016).
54. L. Xi, P.D. Tran, S.Y. Chiam, P.S. Bassi, W.F. Mak, H.K. Mulmudi, S. K. Batabyal, J. Barber, J.S.C. Loo, and L.H. Wong: Co_3O_4-decorated hematite nanorods as an effective photoanode for solar water oxidation. *J. Phys. Chem. C* **116**, 13884 (2012).
55. P.A. Morris Hotsenpiller, J.D. Bolt, W.E. Farneth, J.B. Lowekamp, and G. S. Rohrer: Orientation dependence of photochemical reactions on TiO_2 surfaces. *J. Phys. Chem. B* **102**, 3216 (1998).
56. M.B. Hugenschmidt, L. Gamble, and C.T. Campbell: The interaction of H_2O with a TiO_2(110) surface. *Surf. Sci.* **302**, 329 (1994).
57. H.G. Yang, C.H. Sun, S.Z. Qiao, J. Zou, G. Liu, S.C. Smith, H.M. Cheng, and G.Q. Lu: Anatase TiO_2 single crystals with a large percentage of reactive facets. *Nature* **453**, 638 (2008).
58. G. Liu, C. Sun, H.G. Yang, S.C. Smith, L. Wang, G.Q. Lu, and H.-M. Cheng: Nanosized anatase TiO_2 single crystals for enhanced photocatalytic activity. *Chem. Commun.* **46**, 755 (2010).
59. M. Zhou, S. Zhang, Y. Sun, C. Wu, M. Wang, and Y. Xie: C-oriented and {010} facets exposed $BiVO_4$ nanowall films: template-free fabrication and their enhanced photoelectrochemical properties. *Chem. Asian J.* **5**, 2515 (2010).
60. D. Wang, H. Jiang, X. Zong, Q. Xu, Y. Ma, G. Li, and C. Li: Crystal facet dependence of water oxidation on $BiVO_4$ sheets under visible light irradiation. *Chem. Eur. J.* **17**, 1275 (2011).
61. H.S. Han, S. Shin, D.H. Kim, I.J. Park, J.S. Kim, P.-S. Huang, J.-K. Lee, I. S. Cho, and X. Zheng: Boosting the solar water oxidation performance of a $BiVO_4$ photoanode by crystallographic orientation control. *Energy Environ. Sci.* **11**, 1299 (2018).
62. H. Dotan, K. Sivula, M. Grätzel, A. Rothschild, and S.C. Warren: Probing the photoelectrochemical properties of hematite (α-Fe_2O_3) electrodes

https://doi.org/10.1557/mrc.2018.106 Published online by Cambridge University Press

using hydrogen peroxide as a hole scavenger. *Energy Environ. Sci.* **4**, 958 (2011).
63. Z. Chen, T.F. Jaramillo, T.G. Deutsch, A. Kleiman-Shwarsctein, A. J. Forman, N. Gaillard, R. Garland, K. Takanabe, C. Heske, M. Sunkara, E.W. McFarland, K. Domen, E.L. Milled, and H.N. Dinh: Accelerating materials development for photoelectrochemical hydrogen production: Standards for methods, definitions, and reporting protocols. *J. Mater. Res.* **25**, 3 (2010).
64. C.W. Kim, Y.S. Son, M.J. Kang, D.Y. Kim, and Y.S. Kang: (040)-Crystal facet engineering of $BiVO_4$ plate photoanodes for solar fuel production. *Adv. Energy Mater.* **6**, 1501754 (2016).
65. Z. Chen, H.N. Dinh, and E. Miller: *Photoelectrochemical Water Splitting*. in *Chim. Int. J. Chem.* (Springer New York, New York, NY, 2013), p. 73.
66. P.M. Rao, L. Cai, C. Liu, I.S. Cho, C.H. Lee, J.M. Weisse, P. Yang, and X. Zheng: Simultaneously efficient light absorption and charge separation in $WO_3/BiVO_4$ core/shell nanowire photoanode for photoelectrochemical water oxidation. *Nano Lett.* **14**, 1099 (2014).
67. X. Li, J. Yu, J. Low, Y. Fang, J. Xiao, and X. Chen: Engineering heterogeneous semiconductors for solar water splitting. *J. Mater. Chem. A* **3**, 2485 (2015).
68. W. Zhao, Y. Wang, Y. Yang, J. Tang, and Y. Yang: Carbon spheres supported visible-light-driven CuO-$BiVO_4$ heterojunction: preparation, characterization, and photocatalytic properties. *Appl. Catal. B Environ.* **115**, 90 (2012).
69. R. Saito, Y. Miseki, and K. Sayama: Highly efficient photoelectrochemical water splitting using a thin film photoanode of $BiVO_4/SnO_2/WO_3$ multi-composite in a carbonate electrolyte. *Chem. Commun.* **48**, 3833 (2012).
70. P. Ju, P. Wang, B. Li, H. Fan, S. Ai, D. Zhang, and Y. Wang: A novel calcined $Bi_2WO_6/BiVO_4$ heterojunction photocatalyst with highly enhanced photocatalytic activity. *Chem. Eng. J.* **236**, 430 (2014).
71. S.J. Hong, S. Lee, J.S. Jang, and J.S. Lee: Heterojunction $BiVO_4/WO_3$ electrodes for enhanced photoactivity of water oxidation. *Energy Environ. Sci.* **4**, 1781 (2011).
72. M.G. Lee, D.H. Kim, W. Sohn, C.W. Moon, H. Park, S. Lee, and H. W. Jang: Conformally coated $BiVO_4$ nanodots on porosity-controlled WO_3 nanorods as highly efficient type II heterojunction photoanodes for water oxidation. *Nano Energy* **28**, 250 (2016).
73. J. Resasco, H. Zhang, N. Kornienko, N. Becknell, H. Lee, J. Guo, A. L. Briseno, and P. Yang: $TiO_2/BiVO_4$ nanowire heterostructure photoanodes based on type II band alignment. *ACS Cent. Sci.* **2**, 80 (2016).
74. Y. Pihosh, I. Turkevych, K. Mawatari, T. Asai, T. Hisatomi, J. Uemura, M. Tosa, K. Shimamura, J. Kubota, K. Domen, and T. Kitamori: Nanostructured $WO_3/BiVO_4$ photoanodes for efficient photoelectrochemical water splitting. *Small* **10**, 3692 (2014).
75. X. Chang, T. Wang, P. Zhang, J. Zhang, A. Li, and J. Gong: Enhanced surface reaction kinetics and charge separation of p–n heterojunction $Co_3O_4/BiVO_4$ photoanodes. *J. Am. Chem. Soc.* **137**, 8356 (2015).
76. M. Long, W. Cai, J. Cai, B. Zhou, X. Chai, and Y. Wu: Efficient photocatalytic degradation of phenol over $Co_3O_4/BiVO_4$ composite under visible light irradiation. *J. Phys. Chem. B* **110**, 20211 (2006).
77. J.G. McAlpin, Y. Surendranath, M. Dinca, T. A. Stich, S. A. Stoian, W. H. Casey, D.G. Nocera, R.D. Britt, M. Dincã, T. A. Stich, S. A. Stoian, W.H. Casey, D.G. Nocera, and R.D. Britt: EPR evidence for Co(IV) species produced during water oxidation at neutral pH. *J. Am. Chem. Soc.* **4**, 6882 (2010).
78. J. Wang and F.E. Osterloh: Limiting factors for photochemical charge separation in $BiVO_4/Co_3O_4$, a highly active photocatalyst for water oxidation in sunlight. *J. Mater. Chem. A* **2**, 9405 (2014).
79. J. Li, S.K. Cushing, P. Zheng, F. Meng, D. Chu, and N. Wu: Plasmon-induced photonic and energy-transfer enhancement of solar water splitting by a hematite nanorod array. *Nat. Commun.* **4**, 1 (2013).
80. M.G. Lee, C.W. Moon, H. Park, W. Sohn, S.B. Kang, S. Lee, K.J. Choi, and H.W. Jang: Dominance of plasmonic resonant energy transfer over direct electron transfer in substantially enhanced water oxidation activity of $BiVO_4$ by shape-controlled au nanoparticles. *Small* **13**, 1701644 (2017).
81. L. Zhang, L.O. Herrmann, and J.J. Baumberg: Size dependent plasmonic effect on $BiVO_4$ photoanodes for solar water splitting. *Sci. Rep.* **5**, 1 (2015).
82. S. Linic, P. Christopher, and D.B. Ingram: Plasmonic-metal nanostructures for efficient conversion of solar to chemical energy. *Nat. Mater.* **10**, 911 (2011).
83. M. Valenti and W.A. Smith: Plasmonic nanoparticle-semiconductor composites for efficient solar water splitting. *J. Mater. Chem. A Mater. Energy Sustain.* **4**, 17891 (2016).
84. F.F. Abdi, A. Dabirian, B. Dam, and R. van de Krol: Plasmonic enhancement of the optical absorption and catalytic efficiency of $BiVO_4$ photoanodes decorated with $Ag@SiO_2$ core–shell nanoparticles. *Phys. Chem. Chem. Phys.* **16**, 15272 (2014).
85. N.J. Halas, S. Lal, W. Chang, S. Link, and P. Nordlander: Plasmons in strongly coupled metallic nanostructures. *Chem. Rev.* **111**, 3913 (2011).
86. P. Chatchai, S. ya Kishioka, Y. Murakami, A.Y. Nosaka, and Y. Nosaka: Enhanced photoelectrocatalytic activity of $FTO/WO_3/BiVO_4$ electrode modified with gold nanoparticles for water oxidation under visible light irradiation. *Electrochim. Acta* **55**, 592 (2010).
87. H.M. Chen, C.K. Chen, C.-J. Chen, L.-C. Cheng, P.C. Wu, B.H. Cheng, Y. Z. Ho, M.L. Tseng, Y.-Y. Hsu, T.-S. Chan, J.-F. Lee, R.-S. Liu, and D.P. Tsai: Plasmon inducing effects for enhanced photoelectrochemical water splitting: x-ray absorption approach to electronic structures. *ACS Nano* **6**, 7362 (2012).
88. D. Hu, P. Diao, D. Xu, and Q. Wu: Gold/WO_3 nanocomposite photoanodes for plasmonic solar water splitting. *Nano Res.* **9**, 1735 (2016).
89. M. Wang, M. Ye, J. Iocozzia, C. Lin, and Z. Lin: Plasmon-mediated solar energy conversion via photocatalysis in noble metal/semiconductor composites. *Adv. Sci.* **3**, 1600024 (2015).
90. Y.C. Pu, G. Wang, K. Der Chang, Y. Ling, Y.K. Lin, B.C. Fitzmorris, C. M. Liu, X. Lu, Y. Tong, J.Z. Zhang, Y.J. Hsu, and Y. Li: Au nanostructure-decorated TiO_2 nanowires exhibiting photoactivity across entire UV-visible region for photoelectrochemical water splitting. *Nano Lett.* **13**, 3817 (2013).
91. S. Kundu: A new route for the formation of Au nanowires and application of shape-selective Au nanoparticles in SERS studies. *J. Mater. Chem. C* **1**, 831 (2013).
92. C.W. Moon, S.Y. Lee, W. Sohn, D.M. Andoshe, D.H. Kim, K. Hong, and H.W. Jang: Plasmonic octahedral gold nanoparticles of maximized near electromagnetic fields for enhancing catalytic hole transfer in solar water splitting. *Part. Part. Syst. Charact.* **34**, 1600340 (2017).
93. Y. Liu, X. Yan, Z. Kang, Y. Li, Y. Shen, Y. Sun, L. Wang, and Y. Zhang: Synergistic effect of surface plasmonic particles and surface passivation layer on ZnO nanorods array for improved photoelectrochemical water splitting. *Sci. Rep.* **6**, 1 (2016).
94. S.Y. Jeong, H.-M. Shin, Y.-R. Jo, Y.J. Kim, S. Kim, W.-J. Lee, G.J. Lee, J. Song, B.J. Moon, S. Seo, H. An, S.H. Lee, Y.M. Song, B.-J. Kim, M.-H. Yoon, and S. Lee: Plasmonic silver nanoparticle-impregnated nanocomposite $BiVO_4$ photoanode for plasmon-enhanced photocatalytic water splitting. *J. Phys. Chem. C* **122**, 7088 (2018).
95. J. Li, J. Zhou, H. Hao, and W. Li: Controlled synthesis of Fe_2O_3 modified Ag-(010)$BiVO_4$ heterostructures with enhanced photoelectrochemical activity toward the dye degradation. *Appl. Surf. Sci.* **399**, 1 (2017).
96. C.K. Huang, T. Wu, C.W. Huang, C.Y. Lai, M.Y. Wu, and Y.W. Lin: Enhanced photocatalytic performance of $BiVO_4$ in aqueous $AgNO_3$ solution under visible light irradiation. *Appl. Surf. Sci.* **399**, 10 (2017).
97. D.K. Zhong, M. Cornuz, K. Sivula, M. Grätzel, and D.R. Gamelin: Photo-assisted electrodeposition of cobalt–phosphate (Co–Pi) catalyst on hematite photoanodes for solar water oxidation. *Energy Environ. Sci.* **4**, 1759 (2011).
98. J.A. Seabold and K.S. Choi: Effect of a cobalt-based oxygen evolution catalyst on the stability and the selectivity of photo-oxidation reactions of a WO_3 photoanode. *Chem. Mater.* **23**, 1105 (2011).
99. L. Fang, F. Nan, Y. Yang, and D. Cao: Enhanced photoelectrochemical and photocatalytic activity in visible-light-driven $Ag/BiVO_4$ inverse opals. *Appl. Phys. Lett.* **108**, 93902 (2016).
100. E. Thimsen, F. Le Formal, M. Grätzel, and S.C. Warren: Influence of plasmonic Au nanoparticles on the photoactivity of Fe_2O_3 electrodes for water splitting. *Nano Lett.* **11**, 35 (2011).
101. I. Thomann, B.A. Pinaud, Z. Chen, B.M. Clemens, T.F. Jaramillo, and M.L. Brongersma: Plasmon enhanced solar-to-fuel energy conversion. *Nano Lett.* **11**, 3440 (2011).

https://doi.org/10.1557/mrc.2018.106 Published online by Cambridge University Press

102. K.J. McDonald and K.-S. Choi: A new electrochemical synthesis route for a BiOI electrode and its conversion to a highly efficient porous $BiVO_4$ photoanode for solar water oxidation. *Energy Environ. Sci.* **5**, 8553 (2012).
103. D.K. Zhong, J. Sun, H. Inumaru, and D.R. Gamelin: Solar water oxidation by composite catalyst/r-Fe_2O_3 photoanodes. *J. Am. Chem. Soc.* **131**, 6086 (2009).
104. D.K. Zhong and D.R. Gamelin: Photoelectrochemical water oxidation by cobalt catalyst ("Co-Pi")r-Fe_2O_3 composite photoanodes oxygen evolution and resolution of a kinetic bottleneck.pdf. *J. Am. Chem. Soc.* **132**, 4202 (2010).
105. E.M.P. Steinmiller and K.-S. Choi: Photochemical deposition of cobalt-based oxygen evolving catalyst on a semiconductor photoanode for solar oxygen production. *Proc. Natl. Acad. Sci. USA* **106**, 20633 (2009).
106. J.J.H. Pijpers, M.T. Winkler, Y. Surendranath, T. Buonassisi, and D.G. Nocera: Supporting information light-induced water oxidation at silicon electrodes functionalized with a cobalt oxygen evolving catalyst. *Proc. Natl. Acad. Sci. USA* **108**, 10056 (2011).
107. E.R. Young, R. Costi, S. Paydavosi, D.G. Nocera, and V. Bulović: Photo-assisted water oxidation with cobalt-based catalyst formed from thin-film cobalt metal on silicon photoanodes. *Energy Environ. Sci.* **4**, 2058 (2011).
108. W. Luo, Z. Yang, Z. Li, J. Zhang, J. Liu, Z. Zhao, Z. Wang, S. Yan, T. Yu, and Z. Zou: Solar hydrogen generation from seawater with a modified $BiVO_4$ photoanode. *Energy Environ. Sci.* **4**, 4046 (2011).
109. T.H. Jeon, W. Choi, and H. Park: Cobalt–phosphate complexes catalyze the photoelectrochemical water oxidation of $BiVO_4$ electrodes. *Phys. Chem. Chem. Phys.* **13**, 21392 (2011).
110. C. Sanchez, K.D. Sieber, and G.A. Somorjai: The photoelectrochemistry of niobium doped α-Fe_2O_3. *J. Electroanal. Chem.* **252**, 269 (1988).
111. F. Le Formal, N. Tétreault, M. Cornuz, T. Moehl, M. Grätzel, and K. Sivula: Passivating surface states on water splitting hematite photoanodes with alumina overlayers. *Chem. Sci.* **2**, 737 (2011).
112. M. Zhong, T. Hisatomi, Y. Kuang, J. Zhao, M. Liu, A. Iwase, Q. Jia, H. Nishiyama, T. Minegishi, M. Nakabayashi, N. Shibata, R. Niishiro, C. Katayama, H. Shibano, M. Katayama, A. Kudo, T. Yamada, and K. Domen: Surface modification of CoO_x loaded $BiVO_4$ photoanodes with ultrathin p-type NiO layers for improved solar water oxidation. *J. Am. Chem. Soc.* **137**, 5053 (2015).
113. J. Xie, C. Guo, P. Yang, X. Wang, D. Liu, and C.M. Li: Bi-functional ferroelectric $BiFeO_3$ passivated $BiVO_4$ photoanode for efficient and stable solar water oxidation. *Nano Energy* **31**, 28 (2017).
114. F. Gao, X.Y. Chen, K.B. Yin, S. Dong, Z.F. Ren, F. Yuan, T. Yu, Z.G. Zou, and J.-M. Liu: Visible-light photocatalytic properties of weak magnetic $BiFeO_3$ nanoparticles. *Adv. Mater.* **19**, 2889 (2007).
115. Y. Zhang, A.M. Schultz, P.A. Salvador, and G.S. Rohrer: Spatially selective visible light photocatalytic activity of TiO_2/$BiFeO_3$ heterostructures. *J. Mater. Chem.* **21**, 4168 (2011).
116. W. Zhang, M.M. Yang, X. Liang, H.W. Zheng, Y. Wang, W.X. Gao, G. L. Yuan, W.F. Zhang, X.G. Li, H.S. Luo, and R.K. Zheng: Piezostrain-enhanced photovoltaic effects in $BiFeO_3$/$La_{0.7}Sr_{0.3}MnO_3$/PMN-PT heterostructures. *Nano Energy* **18**, 315 (2015).
117. W. Dong, Y. Guo, B. Guo, H. Li, H. Liu, and T.W. Joel: Enhanced photovoltaic effect in $BiVO_4$ semiconductor by incorporation with an ultrathin $BiFeO_3$ ferroelectric layer. *ACS Appl. Mater. Interfaces* **5**, 6925 (2013).
118. U.S. Department of Energy: DOE Technical Targets for Hydrogen Production from Electrolysis (2015). Available at: https://energy.gov/eere/fuelcells/doe-technical-targets-hydrogen-production-electrolysis (accessed 27 April 2018).
119. K. Sayama and Y. Miseki: Research and development of solar hydrogen production—toward the realization of ingenious photocatalysis-electrolysis hybrid system. *Synthesiology* **7**, 81 (2014).
120. T. Hisatomi and K. Domen: Introductory lecture: sunlight-driven water splitting and carbon dioxide reduction by heterogeneous semiconductor systems as key processes in artificial photosynthesis. *Faraday Discuss.* **198**, 11 (2017).

https://doi.org/10.1557/mrc.2018.106 Published online by Cambridge University Press